

MR Image Reconstruction From Highly Undersampled k-Space Data by Dictionary Learning

Saiprasad Ravishankar*, *Member, IEEE*, and Yoram Bresler, *Fellow, IEEE*

Abstract—Compressed sensing (CS) utilizes the sparsity of magnetic resonance (MR) images to enable accurate reconstruction from undersampled k-space data. Recent CS methods have employed analytical sparsifying transforms such as wavelets, curvelets, and finite differences. In this paper, we propose a novel framework for adaptively learning the sparsifying transform (dictionary), and reconstructing the image simultaneously from highly undersampled k-space data. The sparsity in this framework is enforced on overlapping image patches emphasizing local structure. Moreover, the dictionary is adapted to the particular image instance thereby favoring better sparsities and consequently much higher undersampling rates. The proposed alternating reconstruction algorithm learns the sparsifying dictionary, and uses it to remove aliasing and noise in one step, and subsequently restores and fills-in the k-space data in the other step. Numerical experiments are conducted on MR images and on real MR data of several anatomies with a variety of sampling schemes. The results demonstrate dramatic improvements on the order of 4–18 dB in reconstruction error and doubling of the acceptable undersampling factor using the proposed adaptive dictionary as compared to previous CS methods. These improvements persist over a wide range of practical data signal-to-noise ratios, without any parameter tuning.

Index Terms—Compressed sensing (CS), dictionary learning, image reconstruction, magnetic resonance imaging (MRI), reduced encoding, sparse representation.

I. INTRODUCTION

MAGNETIC resonance imaging (MRI) is a noninvasive and nonionizing imaging technique. Offering a variety of contrast mechanisms, it enables excellent visualization of both anatomical structure and physiological function. Owing to these advantages, MRI is one of the major diagnostic imaging modalities. However, the main limitation of MRI, affecting both clinical throughput and image quality, especially in dynamic imaging applications, is that it is a relatively slow imaging modality. This is because the data in MRI, samples in k-space of the spatial Fourier transform of the object, are acquired

sequentially in time. In spite of advances in scanner hardware and pulse sequences, the rate at which MR data are acquired is limited by MR physics and physiological constraints on RF energy deposition. A variety of MR techniques therefore aim to reduce the number of data required for accurate reconstruction.

Hardware-based, parallel data acquisition (P-MRI) methods (cf. [1]) reduce the number of k-space samples acquired, and use the diversity provided by multiple RF receiver coils to eliminate the resulting aliasing. P-MRI is widely available in commercial systems and plays an important role in clinical practice. However, although tens of receiver coils may be available, P-MRI is nonetheless limited by increased noise and imperfect alias correction to accelerations typically smaller than 3 or 4 fold. A complement to hardware-based acceleration, are algorithmic reduced acquisition MRI methods. These rely on implicit or explicit modeling or constraints on the underlying image or object [2], with some methods even adapting the acquisition to the imaged object [3], [4]. Compressed sensing (CS) is a recent addition to this arsenal, and is the subject of this paper.

The recent theory of CS [5]–[7] (see also [8]–[15] for the earliest versions of CS for Fourier-sparse signals and for Fourier imaging) enables to recover signals/images accurately using significantly fewer measurements than the number of unknowns, or than mandated by traditional Nyquist Sampling. This is possible provided the underlying signal or image is sparse in some transform domain, and the acquisition is incoherent, in an appropriate sense, with the transform. The cost of this improvement is that the reconstruction procedure is nonlinear. More recently, CS theory has been applied to MRI [16]–[21] demonstrating high quality reconstructions from a reduced set of measurements.

The sparsity of MR images in some transform domain (wavelets, finite differences, contourlets, etc.), or equivalently, MR images admitting a sparse representation in some set of signals known as *dictionary*, are key to accurate CS reconstruction. However, compressed sensing MRI (CSMRI) with nonadaptive, global sparsifying transforms, is usually limited in typical MR images to 2.5–3 fold undersampling [22]. The limitations of CSMRI are illustrated in Fig. 1 on a reference MR image of the brain. The CS sampling scheme shown employs variable density random undersampling in k-space by a factor of 20^1 . The CS data acquisition was simulated by downsampling the 2D discrete Fourier transform of the reference image. The reconstruction by a leading CSMRI method [16], with Daubechies wavelets and total variation (TV) as sparsifying

Manuscript received July 29, 2010; revised October 05, 2010; accepted October 05, 2010. Date of publication November 01, 2010; date of current version May 04, 2011. This work was supported in part by the National Science Foundation (NSF) under Grant CCF 06-35234. Asterisk indicates corresponding author.

*S. Ravishankar is with the Department of Electrical and Computer Engineering and the Coordinated Science Laboratory, University of Illinois, Urbana-Champaign, IL 61801 USA (e-mail: ravisha3@illinois.edu).

Y. Bresler is with the Department of Electrical and Computer Engineering and the Coordinated Science Laboratory, University of Illinois, Urbana-Champaign, IL 61801 USA (e-mail: ybresler@illinois.edu).

Color versions of one or more of the figures in this paper are available online at <http://ieeexplore.ieee.org>.

Digital Object Identifier 10.1109/TMI.2010.2090538

¹This large undersampling factor was chosen for easy visualization of the reconstruction error. Significant errors in this CS reconstruction are observed at undersampling factors as low as 3.

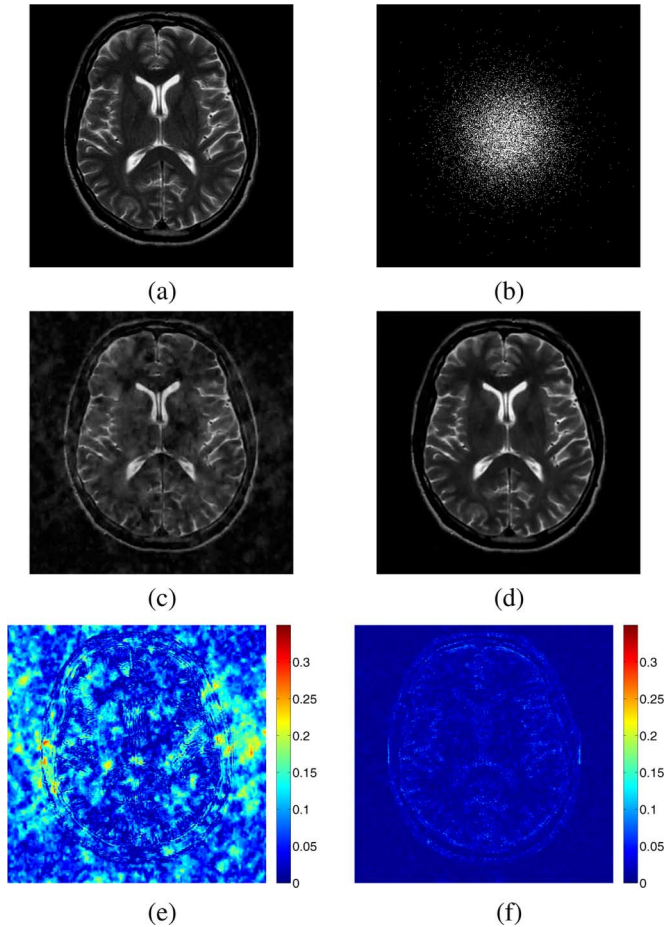


Fig. 1. A comparison of nonadaptive CS versus adaptive patch based CS. (a) Axial T2-weighted reference image of the brain (courtesy: [23]). (b) Sampling mask in k-space with 20 fold undersampling. (c) CSMRI reconstruction [16] with Wavelets and TV. (d) Reconstruction using the proposed adaptive framework. (e) Magnitude of reconstruction error for (c). (f) Magnitude of reconstruction error for (d).

transforms, is clearly seen to have many undesirable artifacts and loss of features. The magnitude of the image reconstruction error (with respect to the reference) also shows many regions of high error.

Adaptive transforms (dictionaries) can sparsify images better since they are learnt for the particular image instance or class of images. Recent studies on adaptive dictionaries [24], [25] have shown the promise of patch-based sparsifying dictionaries in a variety of applications such as image/video denoising, image/video inpainting, deblurring, and demosaicing [26]–[31]. The shift from global image sparsity to patch-based sparsity is appealing since patch based dictionaries can capture local image features effectively, and can potentially remove noise and aliasing artifacts in CSMRI without sacrificing resolution. Patch based schemes have become popular especially in denoising [26], [32] where using overlapping patches can create an additional averaging effect that removes noise. Furthermore, a single image can be decomposed into sufficiently many overlapping patches to train a sparsifying dictionary.

In this work, we exploit adaptive patch-based dictionaries to obtain substantially improved reconstruction performance

for CSMRI. We propose a novel framework for simultaneously learning the dictionary and reconstructing the image from highly undersampled k-space data. Dictionaries adapted to the specific image that is to be recovered have been shown to provide state of the art results in image denoising [30]. Learning a dictionary from a fraction of the image pixels has been studied in the context of image inpainting—that is, filling-in missing or badly corrupted samples in an image [27], [30]. Unlike inpainting, in MRI the available partial data is in k-space rather than in the image domain—a fundamental difference. In this paper, we learn an image-patch dictionary from a small number of k-space samples. Such a measurement-adapted dictionary can give rise to superior sparsities for every image instance thereby leading to substantially higher undersampling rates/speedups for CSMRI. Our approach thus combines the advantages of patch-based dictionaries in a completely adaptive framework making it possible for the reconstruction performance to approach its fundamental limits.

Fig. 1 shows a reconstruction instance using the proposed adaptive dictionary. The result is clearly devoid of the many artifacts seen in the CSMRI reconstruction described earlier and shown in Fig. 1(c) and (e), despite the high undersampling factor. The magnitude of the image reconstruction error [using the same scale as that in the CSMRI reconstruction in Fig. 1(e)] also shows pixel errors of much smaller magnitude.

Our framework can automatically update (adapt) a dictionary learnt *a priori* from a fully sampled reference image(s) to include new features in the current scan data. Additionally, our method can give promising improvements in reconstruction even in the absence of a reference image by directly adapting to the current image content. The dictionary in Fig. 1 was learnt directly from the sampled data without utilizing any reference images. Dispensing with frequent fully-sampled reference images in MRI not only improves throughput, but also enables applications in which it is difficult to acquire relevant reference images.

The implicit goal of CSMRI is to perform accurate k-space interpolation using only a subset of the samples. However, as we determined empirically, explicit k-space interpolation leads to poor reconstructions due to the lack of local structure in k-space. Instead, in this work, we perform implicit interpolation by employing learnt dictionaries in the *image* domain.

The rest of this paper is organized as follows. Section II discusses prior work in CSMRI and dictionary learning. Our problem formulation for MRI reconstruction based on adaptive dictionary learning is detailed in Section III. Section IV discusses the proposed algorithm and its relevant properties. Section V demonstrates the performance of our algorithm on numerous examples, using a variety of sampling schemes and noise levels. In Section VI, we conclude with possible topics for future work.

II. BACKGROUND AND RELATED WORK

We use $x \in \mathbb{C}^P$ to represent as a vector, the P -pixel 2D complex image to be reconstructed, and $y \in \mathbb{C}^m$ represents the k-space measurements. The two are related (in the absence of noise) as $F_u x = y$, where $F_u \in \mathbb{C}^{m \times P}$ is the undersampled Fourier encoding matrix. Undersampling occurs whenever the

number of k-space samples is less than the number of unknowns ($m < P$).

A. CSMRI

Compressed Sensing reconstructs the unknown x from the measurements y , or equivalently solves an underdetermined system of linear equations $F_u x = y$ by minimizing the l_0 quasi norm (i.e., the number of non-zeros) of the sparsified image Ψx , where $\Psi \in \mathbb{C}^{T \times P}$ represents a global, typically orthonormal sparsifying transform for the image. For example, Ψ may be the wavelet transform, so that Ψx corresponds to the wavelet coefficients of x , assumed to be sparse (mostly zero). The corresponding optimization problem is

$$\min_x \|\Psi x\|_0 \quad \text{s.t. } F_u x = y. \quad (1)$$

This l_0 problem, often known as the *sparse coding problem* because it corresponds to finding a sparse code x for the given vector y using the codebook F_u , is NP-hard (nondeterministic polynomial-time hard). However, there are greedy algorithms to solve this problem such as orthogonal matching pursuit (OMP) [11], [33]. Alternatively, the l_0 quasi norm is replaced with its convex relaxation, the l_1 norm [34] at which point the problem can be solved via linear programming [7] in the real case, or via second order cone programming in the complex case. When the measurements are noisy, the CS problem is solved using basis pursuit denoising [35]. Under certain conditions, these algorithms can be guaranteed to provide the correct solution, or provide it with high probability. In practice, these algorithms usually perform better than predicted by the available theory. Other algorithms, for which similar theoretical performance guarantees may not be available, often provide even better empirical performance [36]–[40].

Compressed Sensing has been applied to a variety of MR modalities such as static MRI [16], [19], [20], dynamic MRI [17], [21], [41], [42], and perfusion imaging and diffusion tensor imaging (DTI) [45]. In this paper, we restrict our attention to CS for static MRI and study it in detail.

The typical formulation of the CSMRI reconstruction problem uses l_1 relaxation of the l_0 quasi norm, and accounts for the noise in the k-space measurements in the following Lagrangian setup [16]

$$\min_x \|F_u x - y\|_2^2 + \lambda \|\Psi x\|_1. \quad (2)$$

This problem formulation involves a global sparsity measure and an analytical, fast sparsifying transform Ψ . However, common transforms such as wavelets result in artifacts such as gibbs ringing in the result. Hence, a TV penalty, corresponding to a finite difference approximation to a gradient sparsifying transform, is typically added to the formulation to enforce spatial homogeneity.

Other sparsifying transforms have been proposed for CSMRI including a dual-tree complex wavelet transform [46] and overcomplete contourlets [47]. Wavelets can recover point-like features while contourlets recover curve-like image features. A Combination of wavelets, contourlets, and TV was shown to increase peak signal-to-noise ratio (PSNR) by 1.3 dB over

wavelets + TV [48]. A refinement of the wavelet sparsifying transform uses a Gaussian scale mixture (GSM) model [20] to exploit the dependencies between wavelet coefficients in CSMRI. The effectiveness of this approach is discussed in the next paragraph.

Numerous algorithms to solve the CSMRI reconstruction problem (2) have been presented. Lustig *et al.* [16] solve (2) using a nonlinear conjugate gradient descent algorithm with backtracking line search. The focus of that paper is primarily on cartesian sampling schemes and results are shown for brain imaging and angiography. Ma *et al.* [22] present an algorithm based on an iterative operator-splitting framework that exploits fast wavelet and Fourier transforms to enable fast reconstruction. However, the results shown at higher undersampling factors (>3 times) suffer from many artifacts. Qu *et al.* [49] use the contourlet transform within an efficient soft iterative thresholding algorithm for CSMRI and show improvements of about 1.5 dB over wavelet CSMRI. Kim *et al.* [20] combine the GSM model with iterative hard thresholding (IHT) to perform the reconstruction. However, the improvements shown in this work on *in vivo* data are not quantified and appear small, and only a low undersampling factor (about 2) is used.

In an attempt to improve the performance of CSMRI beyond that obtained using l_1 relaxation or greedy algorithms to encode sparsity, several authors turned to nonconvex relaxations or approximations. Chartrand [18] used the l_p quasi norm (where $0 < p < 1$), which approximates the l_0 quasi norm better than the l_1 norm. For an image of the uterus, $p < 1$ is demonstrated to improve the SNR of the reconstruction by a small amount (of 0.9 dB). Trzasko *et al.* [50], [51] propose an alternative reconstruction based on a homotopic approximation of the l_0 quasi norm. Their algorithm involves iterative alternation between bilateral filtering, and projection of the measured k-space samples. The same authors claim that homotopic l_0 minimization can provide higher undersampling factors than l_1 norm based methods [19]. However, their reconstructions for spine and wrist images still contain some prominent aliasing and other artifacts at the undersampling factors of 4–7.5 simulated.

B. Dictionary Learning

The nonadaptive CSMRI techniques are limited by the degree of undersampling at which they can still give clinically useful reconstructions. Adaptive dictionaries lead to higher sparsities and hence to potentially higher undersampling factors in CSMRI. The key to adapting the dictionary to the data is dictionary learning. Given an image $x \in \mathbb{C}^P$, $x_{ij} \in \mathbb{C}^n$ is the vector representation of the square 2D image patch of size $\sqrt{n} \times \sqrt{n}$ pixels, indexed by the location of its top-left corner, (i, j) , in the image. We use $D \in \mathbb{C}^{n \times K}$ to represent the image patch-based dictionary. The dictionary D has K atoms (columns), each an n -vector corresponding to a $\sqrt{n} \times \sqrt{n}$ “elemental patch.” It is assumed that each patch x_{ij} can be approximated by a linear combination $D\alpha_{ij}$ of dictionary atoms, where $\alpha_{ij} \in \mathbb{C}^K$ is sparse. Accordingly, we say that α_{ij} is the sparse representation of x_{ij} with respect to D . When $K = n$, the number of atoms equals the dimension of a patch, and D is said to be a basis. Otherwise, when $K > n$, the dictionary is said to be overcomplete. Fig. 2 shows an example

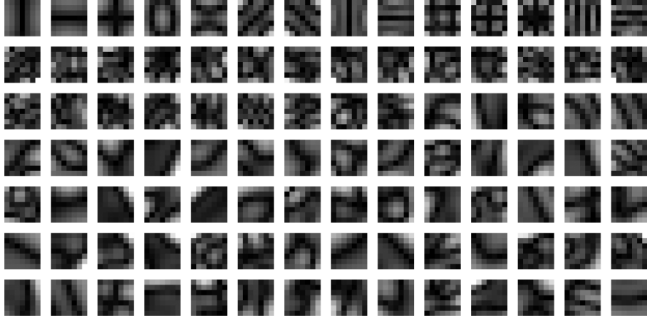


Fig. 2. The atoms of a 49×98 dictionary shown as 7×7 elemental patches. The magnitudes are displayed.

overcomplete dictionary of size 49×98 where the atoms (magnitudes) are displayed as 7×7 elemental patches and are learnt from the 20-fold undersampled k-space data of Fig. 1 using the formulation described later in Section III.

Dictionary Learning (DL) aims to solve the following optimization problem:

$$\min_{D, \Gamma} \sum_{ij} \|R_{ij}x - D\alpha_{ij}\|_2^2 \quad \text{s.t.} \quad \|\alpha_{ij}\|_0 \leq T_0 \quad \forall i, j. \quad (3)$$

Matrix $R_{ij} \in \mathbb{C}^{n \times P}$ represents the operator that extracts the patch x_{ij} from x as $x_{ij} = R_{ij}x$. The l_0 quasi norm is used to encode the sparsity of the patch representation, and T_0 is the required sparsity level. Γ is used to denote the set $\{\alpha_{ij}\}_{ij}$ of sparse representations of all patches. This learning formulation minimizes the total fitting error of all image patches with respect to the dictionary, subject to sparsity constraints.

The DL problem (3) is NP-hard, because for fixed D and x it reduces to the sparse coding problem. However, unlike the latter problem [or equivalently, the compressive sensing problem (1)], even with a convex relaxation of the l_0 quasi norm, the optimization problem for learning is nonconvex in the unknown variables, making it harder. Numerous algorithms have been proposed to solve such a dictionary learning problem [24], [25], [52], [53] (also see survey in [54]). These algorithms typically alternate between finding the dictionary D , and the sparse representations Γ . In particular, the K-SVD algorithm [24] has been widely used in many applications [26]–[28]. It performs the dictionary update step in a sequential manner where each column/atom of D is updated jointly with the corresponding representation coefficients for the patches that currently use it. This sequential update is similar to the one performed in the K-means algorithm but involves computing K Singular Value Decompositions (SVDs); one for each atom. Hence, the name K-SVD.

Dictionary learning for medical imaging has received only recent attention. The learning is typically done using reference images. In an application to ultrasound breast imaging [55], the dictionary is trained from reference MRI scans using maximum likelihood dictionary learning [53], which is an older algorithm than K-SVD.

Bilgin *et al.* [56] learn a K-SVD patch dictionary from a fully sampled reference MRI image slice and use it in IHT to recover undersampled test image slices. However, the k-space undersampling factor used is low (about 2) and the improvement in reconstruction SNR compared to wavelet-IHT is small (1.5 dB).

Chen *et al.* [57] learn a patch-based K-SVD dictionary from fully sampled reference images, and employ the l_1 norm for sparsity in the reconstruction. The results show improved performance with the learnt dictionary over CSMRI with wavelets as sparsifying transform. However, the improvement is small (SNR increases by 1.6 dB compared to CS with wavelets), and the error map shown in the work has considerable structure indicating loss of features in the reconstructed image. These results suggest that a dictionary learnt from a reference image would not be able to effectively sparsify new features in the current scan.

Otazo and Sodickson [58], learn a one dimensional dictionary for MRI using K-SVD, directly from the columns of an initial reconstruction obtained by CSMRI with 1D-Wavelets. In comparison to the CSMRI result, the learned dictionary is shown to produce better reconstruction. However, a 1D dictionary is a very restricted dictionary that cannot exploit the 2D local structure of the image. The number of training patches for such a dictionary would be equal to the number of image columns, which is insufficient for training. As might be therefore expected, the reconstructed image in this work is seen to have visible artifacts even at 2.5 fold undersampling.

III. PROBLEM FORMULATION

The problem formulation for CSMRI based on dictionary learning needs to have two characteristics. It should be able to enforce sparsity of the patches of the reconstructed image in an adaptive dictionary, and produce a reconstruction that is consistent with the available k-space data. It should also be able to avoid artifacts typically seen in the zero-filled Fourier reconstruction. Artifacts arise chiefly due to two reasons: undersampling of k-space, and noise in the samples. Undersampling of k-space causes aliasing in the image domain, and independent and identically distributed (i.i.d.) zero-mean complex Gaussian noise in the measured k-space samples (undersampled) translates to colored Gaussian noise in the image domain.

A possible formulation is

$$(P0) \quad \min_{x, D, \Gamma} \sum_{ij} \|R_{ij}x - D\alpha_{ij}\|_2^2 + \nu \|F_u x - y\|_2^2 \\ \text{s.t.} \quad \|\alpha_{ij}\|_0 \leq T_0 \quad \forall i, j. \quad (4)$$

The first term in the cost function captures the quality of the sparse approximations of the image patches with respect to the dictionary D . The second term in the cost enforces data fidelity in k-space. The patch sparsity constraint is the same as in generic dictionary learning (3). The weight ν in our formulation depends on the standard deviation σ of the measurement noise as $\nu = (\lambda/\sigma)$ where λ is a positive constant. This makes it more robust to noise. Such a form of the weight uses prior knowledge of the measurement process and has been shown to work well in image denoising [30]. Previous CSMRI methods such as [16] without explicit noise adapted data-fidelity weights struggle to enforce a good trade-off between data consistency and denoising. The proposed formulation considers the measurement scenario with known noise level. An estimate of the noise level or the observed noise level can be used when the exact value is unknown.

The problem formulation for the simpler case of noiseless measurements can be obtained by dropping the data fidelity term from the cost and adding it instead as a constraint, $F_u x = y$. This case represents the limiting behavior of Problem (P0) when $\sigma \rightarrow 0$, or $\nu \rightarrow \infty$, and is useful for high SNR of the measurement process.

Our formulation is thus capable of both designing an adaptive dictionary, and also using it to reconstruct the underlying image. This is done using only the undersampled k-space measurements, y . However, just as the generic dictionary learning problem (3), Problem (P0) of simultaneous reconstruction and dictionary learning is NP-hard, and nonconvex even when the l_0 quasi norm is relaxed to an l_1 norm. Alternative (but not necessarily easier) problem formulations can also be generated by modifying Problem (P0). For instance, the sparsity constraints can be combined into the cost function as penalties using Lagrange multipliers. However, in this work, we focus on Problem (P0).

We use periodically positioned, overlapping 2D image patches in our formulation. The *overlap stride* r is defined to be the distance in pixels between corresponding pixel locations in adjacent image patches. The patches are said to have maximum overlap for $r = 1$. In this case, every image pixel (i, j) (except the ones near the right and bottom image boundaries) would be the top-left corner of a square 2D patch. If patches are assumed to “wrap around” at image boundaries, then pixels near the right and bottom image boundaries can also constitute the top-left corners of patches. The patches in this scenario begin near the image boundary and wrap around on the opposite side of the image. When there is “wrap around” and $r = 1$, each pixel in the image belongs to n different patches, where n is the number of pixels in a patch.

The adaptive patch-sparsity based formulation can potentially remove aliasing and noise while also learning local image features effectively. Overlapping patches are used to create an additional averaging effect for artifact removal. These aspects of the formulation make it very useful for the CSMRI setting.

IV. ALGORITHM AND PROPERTIES

A. Algorithm

Problem (P0) is solved using an alternating minimization procedure. In one step of this alternating scheme, x is assumed fixed, and the dictionary and sparse representations of the patches are jointly learnt. In the other step, the dictionary and sparse representations are fixed, and x is updated to satisfy data consistency. These two steps are further detailed in the following subsections.

1) *Dictionary Learning Step:* In this step, Problem (P0) is solved with fixed x . This corresponds to the subproblem

$$(P1) \quad \min_{D, \Gamma} \sum_{ij} \|R_{ij}x - D\alpha_{ij}\|_2^2$$

$$\text{s.t.} \quad \|d_k\|_2 = 1 \quad \forall k, \|\alpha_{ij}\|_0 \leq T_0 \quad \forall i, j. \quad (5)$$

The cost function for learning takes into account the fitting errors of all the overlapping patches using the sparsifying dictionary. Alternatively, similarly to the application of DL in denoising [30], we use only a fraction δ of all patches to train the

dictionary. The columns of the designed dictionary (represented by $d_k, 1 \leq k \leq K$) are additionally constrained to be of unit norm in order to avoid the scaling ambiguity [59]. The K-SVD algorithm [24] is used to learn the dictionary, D . Once the dictionary is learnt, sparse coding is performed on all patches to determine the α_{ij} .

2) *Updating the Reconstruction:* In this step, Problem (P0) is solved with fixed dictionary and sparse representations. The corresponding update problem is

$$(P2) \quad \min_x \sum_{ij} \|R_{ij}x - D\alpha_{ij}\|_2^2 + \nu \|F_u x - y\|_2^2. \quad (6)$$

Problem (P2) is a simple least squares problem admitting an analytical solution. The least squares solution satisfies the normal equation

$$\left(\sum_{ij} R_{ij}^T R_{ij} + \nu F_u^H F_u \right) x = \sum_{ij} R_{ij}^T D \alpha_{ij} + \nu F_u^H y. \quad (7)$$

The superscript H denotes the Hermitian transpose operation, and the superscript T is used instead of H when the operand is real. Solving (7) directly can be tedious because it requires to invert the $P \times P$ matrix premultiplying x . In general, it requires $O(P^3)$ operations which is impractical for $P = 256 \times 256$. Fortunately, the solution simplifies by using the structure of the different quantities.

The term $\sum_{ij} R_{ij}^T R_{ij} \in \mathbb{C}^{P \times P}$ is a diagonal matrix, where the diagonal entries correspond to image pixel locations and their values are equal to the number of overlapping patches contributing at those pixel locations. The diagonal entries become all equal, and $\sum_{ij} R_{ij}^T R_{ij} = \beta I_P$ (where $I_P \in \mathbb{C}^{P \times P}$ is an identity matrix), if we assume that patches wrap around at image boundaries. In particular, $\beta = n$ when the overlap stride $r = 1$ for the patches. When patches are restricted to the field-of-view (FOV) (no wrap around), the number of patches contributing to pixels near image boundaries would be less than the number contributing to pixels in the rest of the image and $\sum_{ij} R_{ij}^T R_{ij} \approx \beta I_P$. The ‘wrap around’ assumption has been used before for dictionary design [29], and we use it here as well in order to arrive at a simple solution.

The term $\sum_{ij} R_{ij}^T D \alpha_{ij}$ with an additional scaling of $(1/\beta)$ represents the patch averaged result. The patches having been approximated by the learnt dictionary are averaged at their respective locations in the image. The intensity value at each pixel is obtained by averaging the contributions of the various patches that cover it.

The next simplification is obtained by transforming from image space to Fourier space. Let $F \in \mathbb{C}^{P \times P}$ denote the full Fourier encoding matrix normalized such that $F^H F = I_P$. Then, Fx represents the full k-space data. Substituting into (7) yields

$$\left(F \sum_{ij} R_{ij}^T R_{ij} F^H + \nu F F_u^H F_u F^H \right) Fx$$

$$= F \sum_{ij} R_{ij}^T D \alpha_{ij} + \nu F F_u^H y. \quad (8)$$

Algorithm 1

Input : y - k-space measurements
Output : x - Reconstructed MR image
Initialization : $x = x_0 = F_u^H y$
Iteration :

- 1) Learn dictionary and sparse representations for patches of x
- 2) Update x : Each pixel value obtained by averaging contributions of patches that cover it
- 3) $S \leftarrow FFT(x)$
- 4) Restore Sampled frequencies to update S per (9)
- 5) $x \leftarrow IFFT(S)$

Fig. 3. Algorithm to reconstruct MR images from undersampled k-space measurements using adaptive dictionaries.

The matrix $FF_u^H F_u F^H$ is a diagonal matrix consisting of ones and zeros. The ones are at those diagonal entries that correspond to sampled locations in k-space. Vector $FF_u^H y$ represents the zero-filled Fourier measurements. Under the ‘wrap around’ assumption, $F \sum_{ij} R_{ij}^T R_{ij} F^H = \beta I_P$ and the matrix pre-multiplying Fx in (8) becomes diagonal and trivially invertible. Both sides of the equation can be divided by the constant β , and the constant can be absorbed into the weight ν (using $\lambda' = (\lambda/\beta)$).

The ‘patch averaged result’ is transformed to the Fourier domain producing

$$S = \frac{F \sum_{ij} R_{ij}^T D \alpha_{ij}}{\beta}.$$

The solution to (8) is then

$$Fx(k_x, k_y) = \begin{cases} S(k_x, k_y), & (k_x, k_y) \notin \Omega \\ \frac{S(k_x, k_y) + \nu S_0(k_x, k_y)}{1 + \nu}, & (k_x, k_y) \in \Omega \end{cases} \quad (9)$$

where $Fx(k_x, k_y)$ represents the updated value at location (k_x, k_y) , $S_0 = FF_u^H y$ represents the zero-filled k-space measurements, and Ω represents the subset of k-space that has been sampled.

Equation (9) uses the dictionary interpolated values for the nonsampled Fourier frequencies, and fills back the sampled frequencies, albeit with averaging in the presence of noise. For the noiseless case ($\nu \rightarrow \infty$), the sampled frequencies are merely restored to their measured values by this operation. The reconstruction, x , is then obtained by IFFT of Fx .

The proposed algorithm is summarized in Fig. 3. The algorithm is initialized with a zero-filled Fourier reconstruction, $F_u^H y$. If the sampling scheme is non-Cartesian, this is computed rapidly with FFTs using gridding [60]. Simple FFT without gridding sufficed for the pseudo-radial sampling pattern employed in the numerical experiments in Section V, because the samples are chosen to fall on a Cartesian grid. Recall that it was assumed that patches wrap around at image boundaries to arrive at this elegant solution. The proposed algorithm outline of Fig. 3 was implemented with patches being restricted to the FOV. We noticed little difference in reconstructions obtained this way as compared to solving (7) using a conjugate gradients iterative solver. The latter method is considerably slower.

B. Convergence

The proposed algorithm alternates between learning the dictionary and sparse representations, and estimating the reconstruction. Solving Problems (P1) and (P2) iteratively leads to monotonic decrease in the cost function of (P0). Since, the cost function is nonnegative, it converges. Thus, better sparse reconstructions [in the sense of the cost function of (P0)] are learnt at each iteration beginning with the zero-filled result. Empirically (see Section V), the iterates x^k (indexed by iteration number) converge as well but this is yet to be proved rigorously. Another open question involves conditions for perfect reconstruction (in the zero noise case). Numerical experiments suggest that the algorithm can enable perfect reconstruction at reasonably higher undersampling factors than current CSMRI methods.

The stopping criterion for the algorithm can be the value of the objective function. It can also be the norm of the reconstruction difference between successive iterations. Simulations presented in Section V show that the algorithm converges rapidly and a fixed number of iterations can suffice in practise.

C. Parameters

The algorithm has a few design parameters, notably the size of patches ($\sqrt{n} \times \sqrt{n}$), sparsity threshold for each patch (T_0), the number of atoms or degree of overcompleteness of the dictionary (K), fraction of patches used for training (δ), patch overlap stride (r), and the factor λ in the data consistency weight. We study the sensitivity of the algorithm to these parameters empirically in Section V.

D. Algorithm Complexity

The algorithm alternates back and forth between the image domain and k-space. The solution to Problem (P1) involves learning the dictionary D from a fraction δ of all N patches and using it to obtain sparse approximations of the N patches. The dictionary learning (DL) step uses the K-SVD algorithm and employs OMP for sparse coding. The computation is dominated by sparse coding which scales as $O(\delta N K n T_0 J)$ where J is the number of iterations in learning. The cost of sparse coding all N patches using the learnt dictionary is $O(K n T_0 N)$. The costs of DL and the final sparse coding step are balanced by choosing $\delta J = 1$. The computational complexity of the reconstruction update step (P2) is dominated by 2 FFTs which have a cost of $O(P \log P)$. The other computations for (P2) namely patch averaging and sampled frequency averaging are usually faster, low complexity operations.

Under the assumptions of patch ‘wrap around’ and overlap stride $r = 1$, the number of patches $N = P$, and $O(K n T_0 P) \gg O(P \log P)$ typically. This indicates that Problem (P1) dominates the computational cost and the main speed bottleneck is due to the various sparse coding steps within (P1). Using faster sparse coding algorithms along with parallel processing of patches can improve speed significantly. Reduction in the number of overlapping patches by increasing the overlap stride r ($N = P/r^2$, with patch ‘wrap around’), can reduce the complexity further. Other parameters such as patch size, sparsity, and number of dictionary atoms may compromise the solution if made too low.

V. EXPERIMENTS

A. Framework

In this section, the performance of the proposed algorithm is demonstrated at a variety of undersampling factors, with and without noise. The images used in the experiments are *in vivo* MR scans of size 512×512 (many of which are courtesy: [23]). Sampling schemes used in the experiments include 2D random sampling [19], Cartesian sampling with random phase encodes (1D random), and pseudo radial sampling [57]. In the latter scheme, samples are taken on a 512×512 Cartesian grid, at the points nearest to radial lines uniformly spaced in angle. Similarly to prior work on CSMRI [18]–[20], [22], [58] the CS data acquisition was simulated by subsampling the 2D discrete Fourier transform of the MR images (except in Figs. 8 and 10 where pulse sequences were used). The reference MR images (intensities) for the simulated experiments were normalized to a maximum magnitude of 1. Our reconstruction method is compared with a leading CSMRI method by Lustig *et al.* [16] (denoted as LDP), and the baseline zero-filling reconstruction. Other CSMRI methods reviewed in Section II offer only small improvements over LDP [16] and are hence, not included in our comparisons. All implementations were coded in Matlab v7.8 (R2009a). Computations were performed with an Intel Core i5 CPU at 2.27 GHz and 4GB memory, employing a 64-bit Windows 7 operating system. The Matlab implementation of LDP [16] available from the author's website [61], was used in our comparisons. We used the built-in parameter settings in that implementation which performed optimally in our experiments.

In the experiments with or without noise, the nominal values of the various parameters were set as $n = 36$, $K = n = 36$, $T_0 = 0.15 \times n \approx 5$, $\lambda = 140$. We worked with maximum patch overlap, $r = 1$. The learning stage (K-SVD) employed 10 iterations, $200 \cdot K$ patches, and a fixed sparsity of T_0 . The K-SVD learning scheme requires an initialization for the dictionary [24]. We used the left singular vectors of the training data to form the initial 36×36 dictionary. Alternative initializations involving analytical dictionaries such as wavelets were also observed to work well. After learning, the overlapping patches were each sparse coded using the sparsity threshold of T_0 .

Real-valued dictionaries (as in [57]) were used for the simulated experiments with real-valued images and complex-valued dictionaries were used for the actual MR data experiments (Figs. 8 and 10), in which the reconstructed image is usually complex. Complex dictionaries usually yield similar results for the real-valued simulation cases but typically with some more iterations. The algorithm was run for about 10–15 iterations for the simulated experiments, and for a few tens of iterations in Figs. 8 and 10. Currently, the algorithm has an average run time of about 1.4 min per iteration with complex dictionaries. We expect this time to decrease substantially with conversion of the code to C/C++, code optimization, and graphics processing unit (GPU) implementation.

The quality of the reconstruction is quantified using two metrics—PSNR, and a high frequency error norm. PSNR in decibels (dB) is computed as the ratio of the peak intensity value of the reference image to the root mean square (RMS) reconstruction error relative to the reference image. This is a

standard image quality measure in work on image compression and has been used in CSMRI before [49], along with the related metric of SNR (in db) [18], [56]. The high-frequency error norm (HFEN) is used to quantify the quality of reconstruction of edges and fine features. We employ a rotationally symmetric LoG (Laplacian of Gaussian) filter to capture edges. The filter kernel is of size 15×15 pixels, and has a standard deviation of 1.5 pixels. HFEN is computed as the l_2 norm of the result obtained by LoG filtering the difference between the reconstructed and reference images. Needless to say, these metrics do not necessarily represent perceptual visual quality, which can only be accurately assessed by human visual observer studies. Nonetheless, large differences in these metrics typically correspond to visually perceptible differences.

B. Noiseless Case

The noiseless scenario (Problem P0 with $\nu \rightarrow \infty$) can be solved by performing a direct frequency fill-in/restore at the reconstruction update step of our algorithm. One can also solve Problem P0 with a large value for ν . We study the noiseless scenario first in order to see the best, or ideal performance that can be obtained with our formulation and algorithm.

Fig. 4 shows the performance of the algorithm on a brain image employing 2D variable density random sampling of k-space at five fold undersampling. The zero-filled Fourier reconstruction has significant undesirable artifacts due to aliasing. The LDP algorithm [16], [61] is unable to remove the aliasing well. Some of the artifacts in the zero-filled reconstruction persist in the CSMRI-LDP result. This phenomenon can also be seen in later Figs. 6, 9, 11, 10. In contrast, the result with dictionary learning (DLMRI) is seen to be free from artifacts and close to perfect reconstruction. Our algorithm was executed with a fixed number of 10 iterations for this case, to study its performance. The reconstruction error magnitude, i.e., $|x_{\text{Recon}} - x_{\text{Ref}}|$, was thresholded at 5% of the maximum reference image intensity for both the LDP method [16], [61] and DLMRI. This helps identify regions of high error which are overlaid on the reference image in green. The CSMRI result [16], [61] can be seen to have more than 5% error magnitude in many regions (more than 50% of image) while the DLMRI result is almost free of such high magnitude errors (only 0.07% of all pixels).

The norm of the reconstruction difference between successive iterations ($\|x^k - x^{k-1}\|_2$) can be seen to converge quickly. The PSNR for DLMRI after 10 iterations of the algorithm is nearly 18 dB higher than the corresponding value for the LDP method [16], [61]. As expected, the zero-filling reconstruction has the worst PSNR. HFEN is also lower for DLMRI than for LDP [16], [61] indicating the superior performance of DLMRI in capturing edges and fine features. DLMRI was also observed to reconstruct the nonsampled frequencies in k-space much better than LDP [16], [61]. The reconstruction x , showed very little visual change after 5 or 6 iterations of the algorithm. The various plots also show fast convergence and thus, quantitatively demonstrate this fact.

In Fig. 5, variable density cartesian sampling with four fold undersampling is employed on a noncontrast MRA of the Circle of Willis. The reconstruction with DLMRI is clearer, sharper

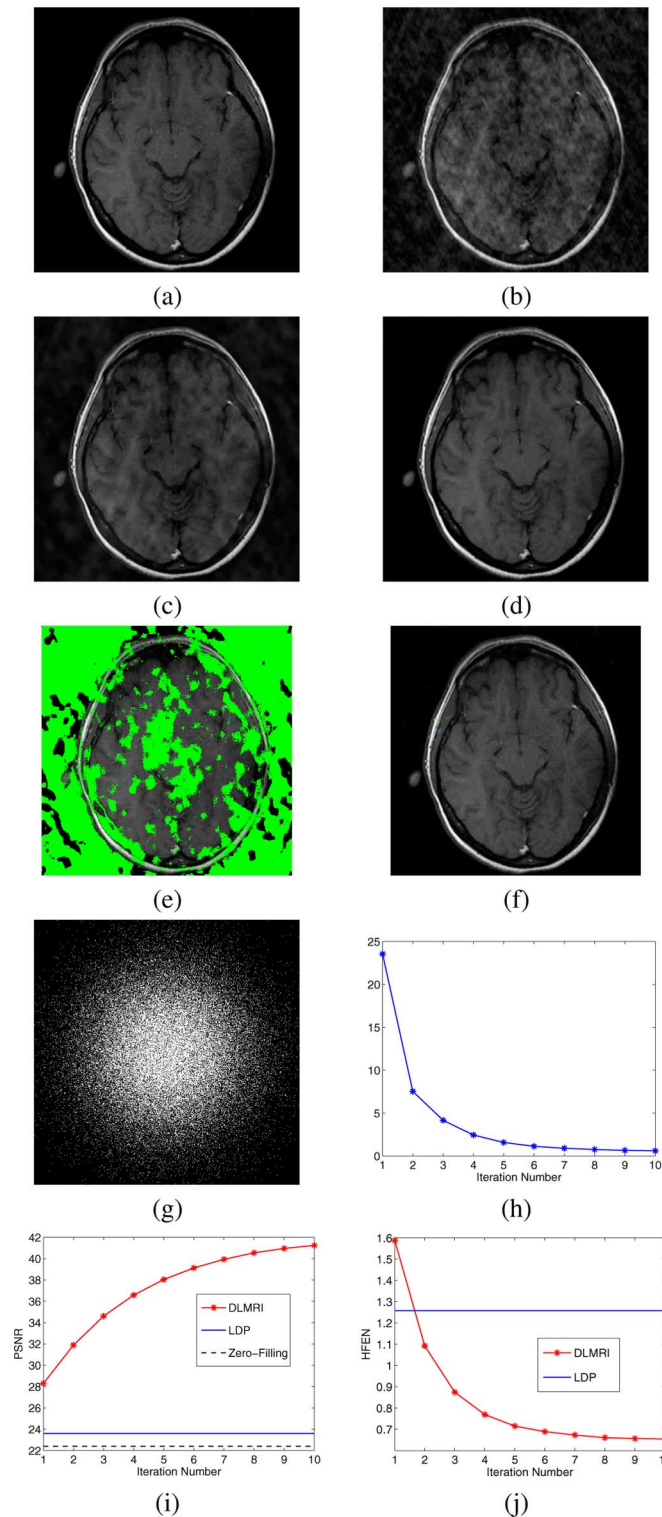


Fig. 4. Performance of algorithm. (a) The reference MR image of the brain. (b) Reconstruction with zero-filling at five fold undersampling. (c) Reconstruction using LDP [16], [61] with Wavelets and TV. (d) Reconstruction using DLMRI. (e) Regions of high error ($>5\%$) overlaid on the reference image in green for LDP [16], [61]. (f) Regions of high error overlaid on the reference image in green for DLMRI (zoom-in is required to view them). (g) Sampling mask in k-space. (h) Norm of the reconstruction difference between successive iterations. (i) PSNR versus iterations with comparison to LDP [16], [61] and zero-filling. (j) HFEN versus iterations with comparison to LDP [16], [61].

than with LDP [16], [61], and relatively devoid of aliasing artifacts. In particular, the vessels in the bottom half of the DLMRI

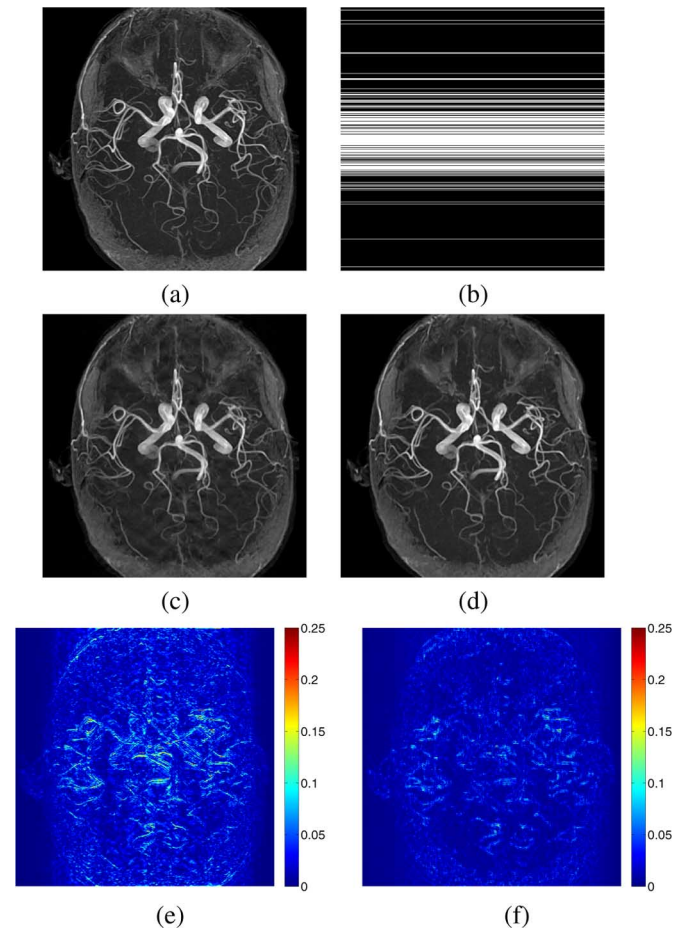


Fig. 5. Cartesian sampling. (a) Reference noncontrast MRA of the Circle of Willis. (b) Sampling mask in k-space with 4 fold undersampling. (c) Reconstruction using LDP [16], [61] with Wavelets and TV. (d) Reconstruction using DLMRI. (e) Reconstruction error magnitude for LDP [16], [61]. (f) Reconstruction error magnitude for DLMRI.

reconstruction appear less obscured than those in the LDP [16], [61] result. The magnitudes of the reconstruction errors for DLMRI and LDP [16], [61] are shown on the same scale. The error image of LDP [16], [61] is seen to have significantly more structured errors indicating loss of features.

In Fig. 6, Cartesian sampling is employed with 7.11 fold undersampling. LDP [16], [61] is unable to remove the large aliasing artifacts seen in the zero-filling result. DLMRI, on the other hand produces an alias-free reconstruction that looks close to the reference. The PSNR and HFEN error metrics also demonstrate the promising performance of DLMRI for this case. A small degree of smoothing in the reconstruction as compared to the reference appears however, inevitable at high undersampling factors as perfect k-space interpolation may not be achieved.

A low resolution reconstruction obtained by sampling the central k-space (Cartesian) phase encoding lines at 7.11 fold undersampling is also shown in Fig. 6. This reconstruction with a PSNR of 29.5 dB has some visible ringing artifacts marked with green arrows. The DLMRI algorithm when executed with only the central k-space data produced a result with a PSNR of 30.7 dB. The small improvement is due to the complete absence of high frequency information in the phase encoding

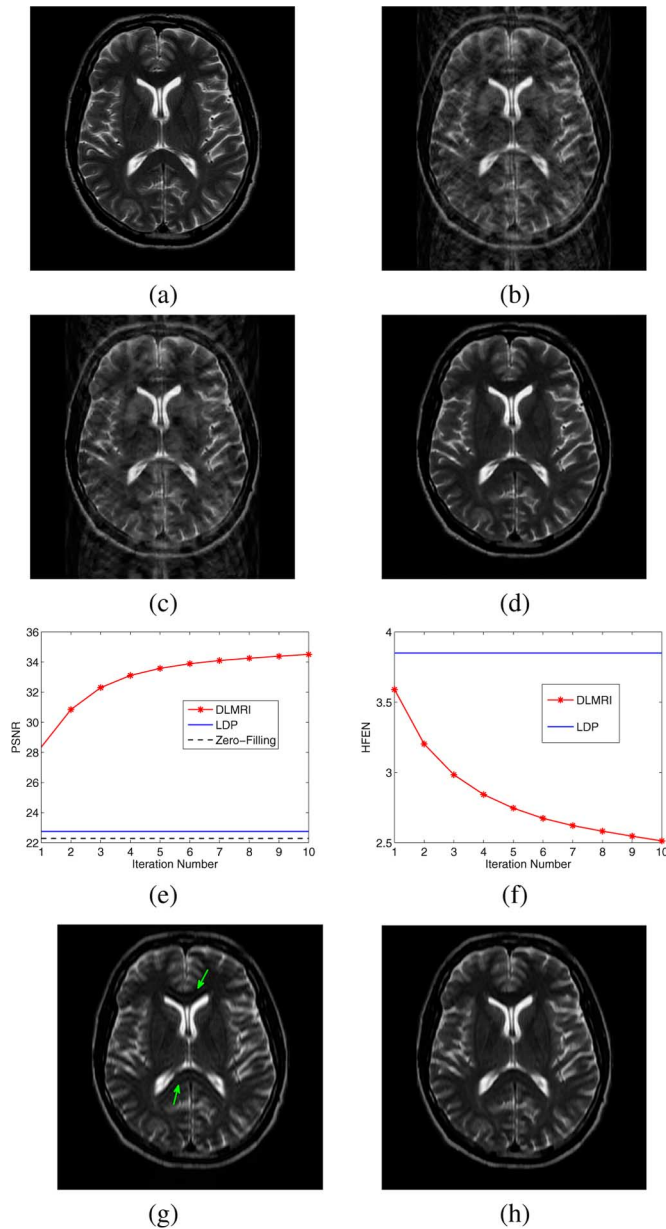


Fig. 6. Cartesian sampling. (a) Reference image. (b) Reconstruction with zero-filling at 7.11 fold undersampling. (c) Reconstruction using LDP [16], [61] with Wavelets and TV. (d) Reconstruction using DLMRI. (e) PSNR versus iterations with comparison to LDP [16], [61] and zero-filling. (f) HFEN versus iterations with comparison to LDP [16], [61]. (g) Low resolution reconstruction. (h) Result of applying DLMRI on low resolution k-space data.

direction. However, some ringing is reduced compared to the low resolution reconstruction due to the local sparsity constraint employed in our formulation. On the other hand, the LDP [16], [61] result (not shown here) had a poorer PSNR of 29.3 dB for this case.

Fig. 7 shows results for the same image and undersampling factor as in Fig. 6 but employing variable density 2D random sampling and pseudo radial sampling [also employed and shown later in Fig. 11(c)], respectively. The DLMRI method for both these sampling schemes is seen to outperform LDP [16], [61]. The adaptive dictionary produces a more significant reduction in aliasing artifacts (i.e., incoherent aliasing artifacts for 2D

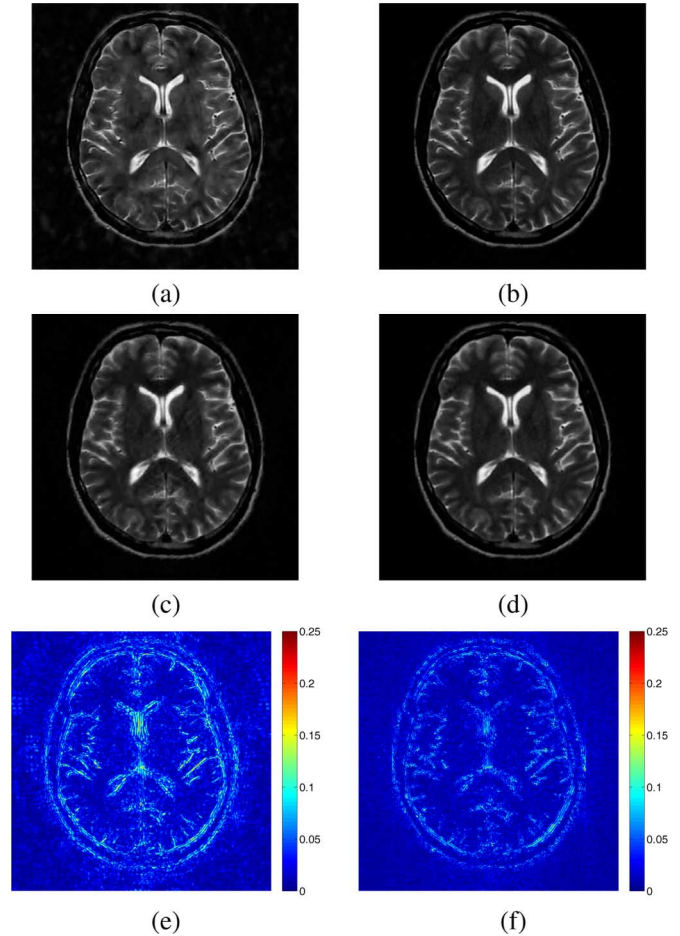


Fig. 7. 2D random, pseudo radial sampling at about 7.11 fold undersampling: (a) Reconstruction using LDP [16], [61] with Wavelets and TV for 2D random sampling. (b) Reconstruction using DLMRI for 2D random sampling. (c) Reconstruction using LDP [16], [61] with Wavelets and TV for pseudo radial sampling. (d) Reconstruction using DLMRI for pseudo radial sampling. (e) Magnitude of reconstruction error for LDP [16], [61] with pseudo radial sampling. (f) Reconstruction error magnitude for DLMRI with pseudo radial sampling.

random sampling, and streaking artifacts for pseudo radial sampling) compared to nonadapted ones. The magnitudes of the reconstruction errors displayed for the pseudo-radial sampling case are also smaller for DLMRI compared to LDP [16], [61]. Figs. 6 and 7 show that DLMRI can perform well with a variety of sampling schemes at a given undersampling factor.

In Fig. 8, T2-weighted k-space data of a brain was acquired using a Cartesian FSE sequence. Randomly undersampled phase encodes of the 2D FSE were obtained in order to test the performance of the proposed reconstruction algorithm. This data was collected by the authors of [16] and made available at the author's website [61]. The reconstructions with the LDP [16], [61] and DLMRI methods at 2.5 fold undersampling do not show much visual difference. However, when the phase encodes were undersampled further, the reconstructions with the two methods displayed notable differences in visual quality. While the LDP [16], [61] reconstructions at 4 and 5 fold undersampling display visible aliasing artifacts along the phase encoding direction (horizontal in the image plane), the DLMRI reconstructions are clear and artifact free at these higher undersampling factors.

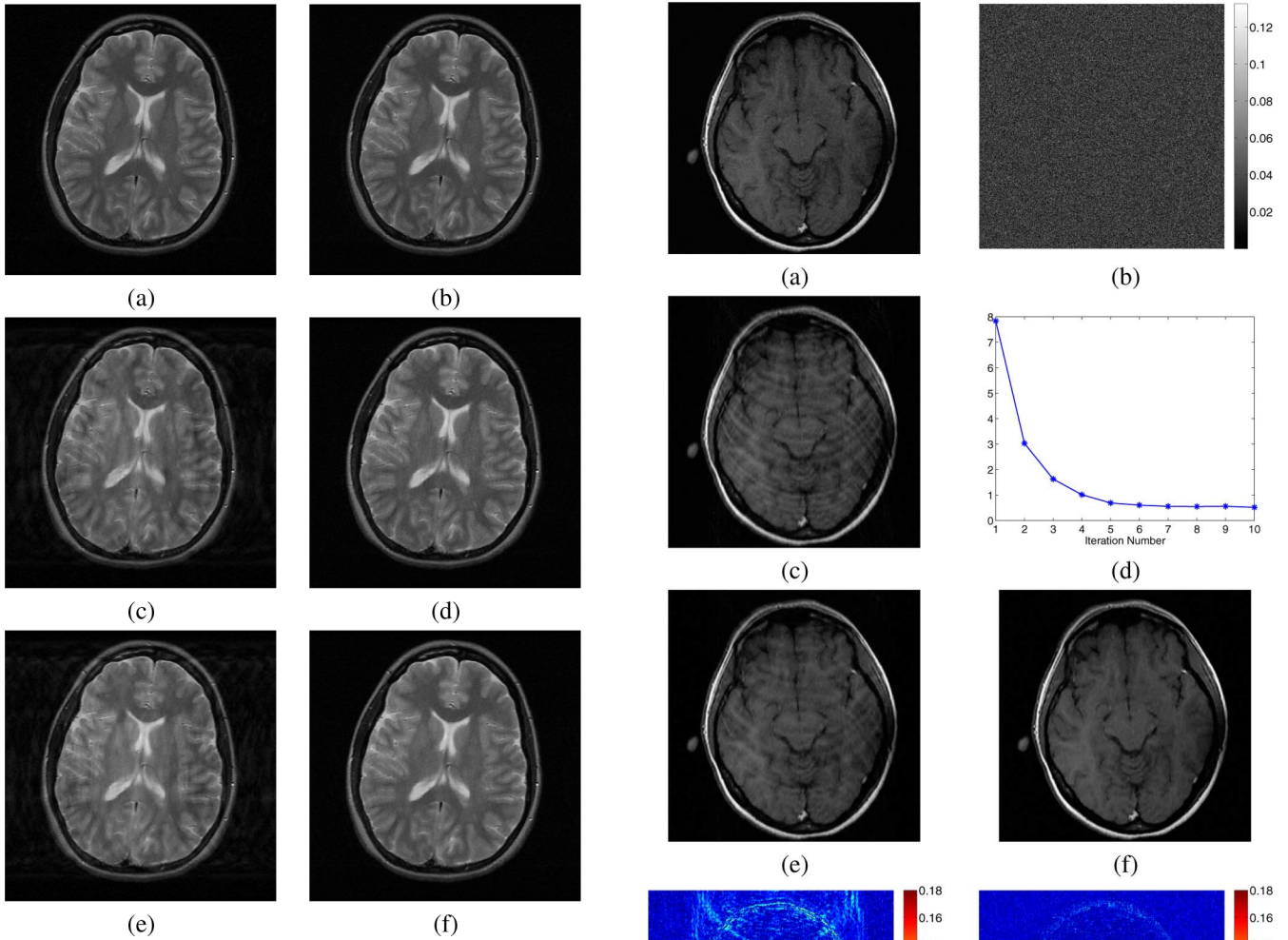


Fig. 8. Cartesian sampling. (a) Reconstruction using LDP [16], [61] with wavelets and TV at 2.5 fold undersampling. (b) Reconstruction using DLMRI at 2.5 fold undersampling. (c) Reconstruction using LDP [16], [61] with wavelets and TV at 4 fold undersampling. (d) Reconstruction using DLMRI at 4 fold undersampling. (e) Reconstruction using LDP [16], [61] with Wavelets and TV at 5 fold undersampling. (f) Reconstruction using DLMRI at 5 fold undersampling.

C. Performance With Noise

The noisy case involves weighted averaging in k-space during the reconstruction update step of the algorithm (9). Fig. 9 demonstrates the performance of our algorithm on the reference image of Fig. 4 using cartesian sampling at 5.23 fold undersampling. Zero-mean complex white Gaussian noise of standard deviation, $\sigma = 18.8$ was added in k-space. The fully sampled noisy image is shown along with the magnitude of the noise-only image, and can be observed to be considerably noisy compared to the reference. The PSNR of the noisy image with respect to the reference is about 30.68 dB. The reconstruction with LDP [16], [61] is unable to sufficiently remove the aliasing and noise seen in the zero-filled result. Our algorithm, on the other hand provides a good reconstruction. The magnitude image of the reconstruction error for DLMRI shows pixel errors of much smaller magnitude and less structure than that of LDP [16], [61].

The PSNR of the DLMRI result (with respect to the noise-free reference) is about 4.1 dB higher than that of LDP [16], [61].

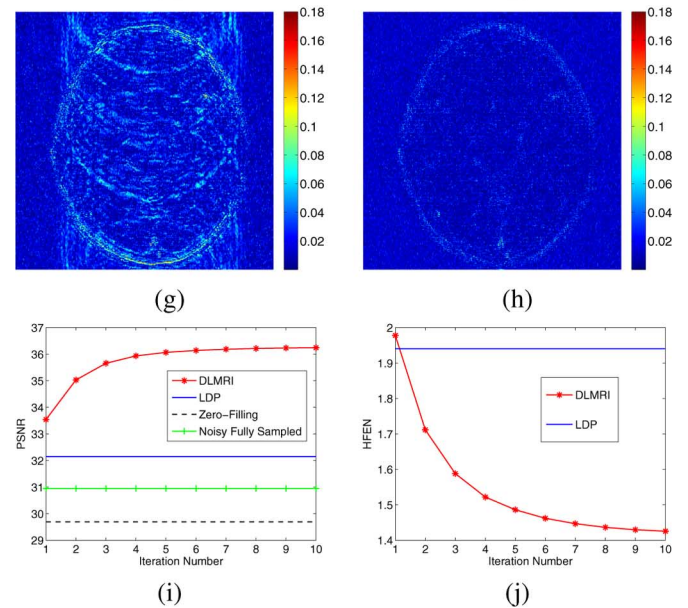


Fig. 9. Performance of algorithm. (a) The fully sampled noisy reconstruction. (b) Noise magnitude in (a). (c) Reconstruction with zero-filling at 5.23 fold undersampling. (d) Norm of the reconstruction difference between successive iterations. (e) Reconstruction using LDP [16], [61] with Wavelets and TV. (f) Reconstruction using DLMRI. (g) Magnitude of reconstruction error for LDP [16], [61]. (h) Reconstruction error magnitude for DLMRI. (i) PSNR versus iterations with comparison to LDP [16], [61], and zero-filling. (j) HFEN versus iterations with comparison to LDP [16], [61].

It is also higher than the PSNR of both the fully sampled noisy image and the zero-filled result indicating good denoising

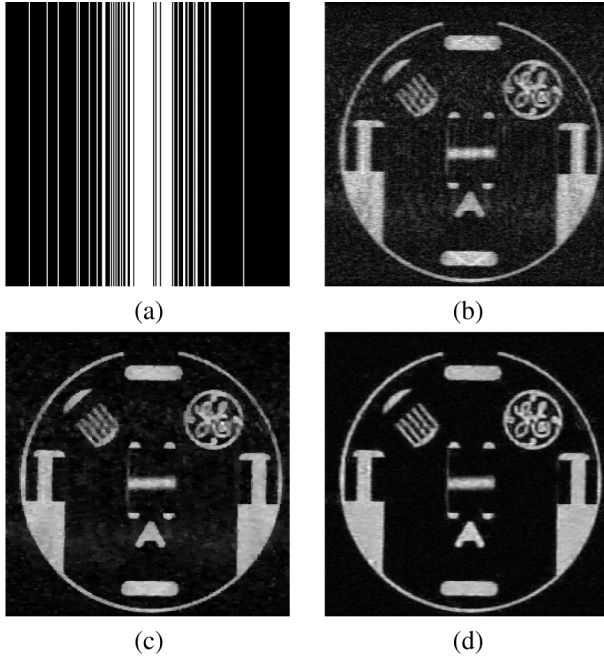


Fig. 10. Cartesian sampling with noisy data. (a) Sampling scheme with 4 fold undersampling. (b) Zero-filled reconstruction. (c) Reconstruction using LDP [16], [61] with TV. (d) Reconstruction using DLMRI.

and aliasing removal. The HFEN metric is also better for DLMRI. The results indicate the promising performance of our formulation/algorithm in the presence of reasonable amount of noise. The algorithm was executed with 10 iterations and the convergence is as rapid as for some of the previous noiseless cases.

In Fig. 10, a phantom (256×256) was scanned using a 2D Cartesian GRE sequence. The scanned data was noisy and is available at [61] (also used by [16]). The k-space was undersampled by a factor of 4 by randomly choosing phase-encode lines. The parameter ν was set at 0.7 based on the observed noise. The reconstruction with LDP [16], [61] retains some of the artifacts seen in the zero-filled reconstruction. On the other hand, the DLMRI reconstruction displays some of the image features better and is clearer, alias free. It is also less noisy compared to the LDP [16], [61] result which shows the superior denoising ability of our framework.

Fig. 11 involves a T2-weighted sagittal view of the Lumbar spine with pseudo radial sampling and 6.09 fold undersampling of the k-space data. Complex Gaussian noise of $\sigma = 14.2$ was added to k-space. The DLMRI reconstruction is seen to be better than that of LDP [16], [61]. Some regions of error in the LDP [16], [61] result have been indicated with arrows. The corresponding regions in the DLMRI reconstruction are clearer and sharper. The magnitude image of the reconstruction error shows pixel errors of lower magnitude and less structure for DLMRI than for LDP [16], [61]. The trends in PSNR and HFEN were similar to Fig. 9 with the exception that the PSNR for the LDP [16], [61] method (29.25 dB) was worse than that of the fully sampled noisy image (34.26 dB). The PSNR for DLMRI (35.6 dB) was 6.35 dB higher than that of LDP [16], [61], and 1.34 dB better than that of the fully sampled noisy image, in spite of using less than 1/6th of the data.

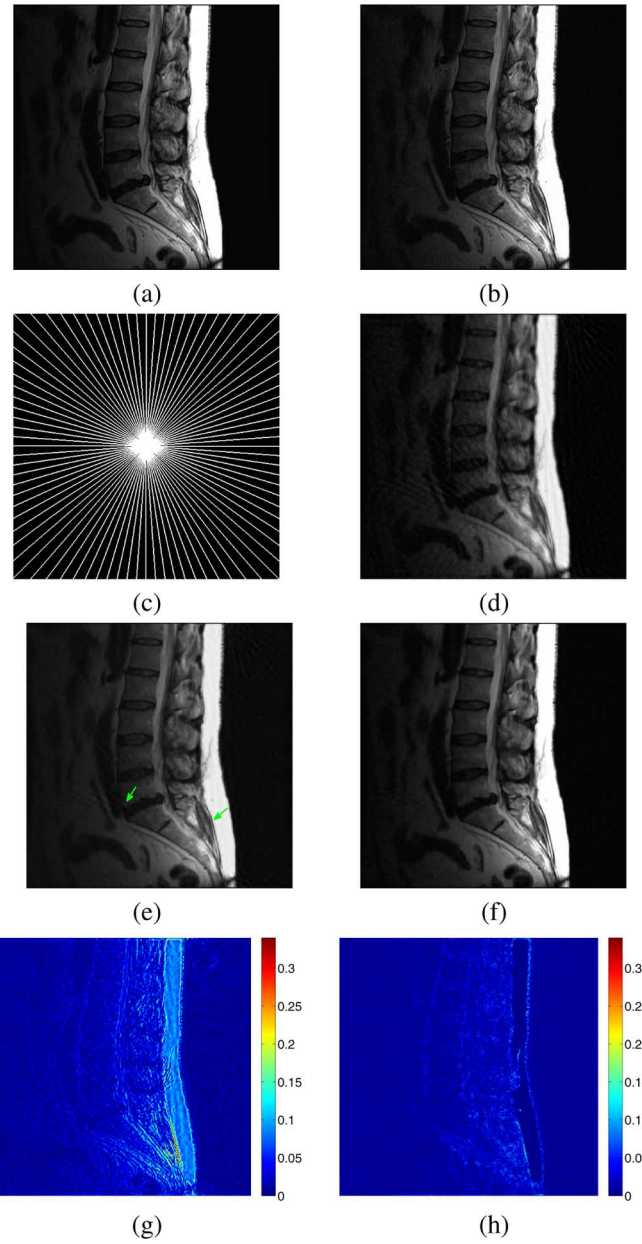


Fig. 11. Pseudo radial sampling. (a) Reference T2-weighted sagittal view of the lumbar spine. (b) The noisy fully sampled reconstruction. (c) Sampling mask in k-space with 6.09 fold undersampling. (d) Reconstruction with zero-filling. (e) Reconstruction using LDP [16], [61] with wavelets and TV (some reconstruction errors pointed with arrows). (f) Reconstruction using DLMRI. (g) Reconstruction error magnitude for (e). (h) Reconstruction error magnitude for (f).

D. Evaluation of Undersampling Limit

In this experiment, the effective undersampling limit achievable with DLMRI as compared to LDP [16], [61] is evaluated. The reference image in Fig. 6 was used for the evaluation with 2D random sampling. Complex white Gaussian noise of $\sigma = 10.2$ was added to the k-space samples. The PSNR of the fully sampled noisy image was 35.3 dB. Reconstructions with DLMRI and LDP [16], [61] methods were obtained at numerous k-space undersampling factors. The variation of PSNR and HFEN as a function of the undersampling factor is shown in Fig. 12.

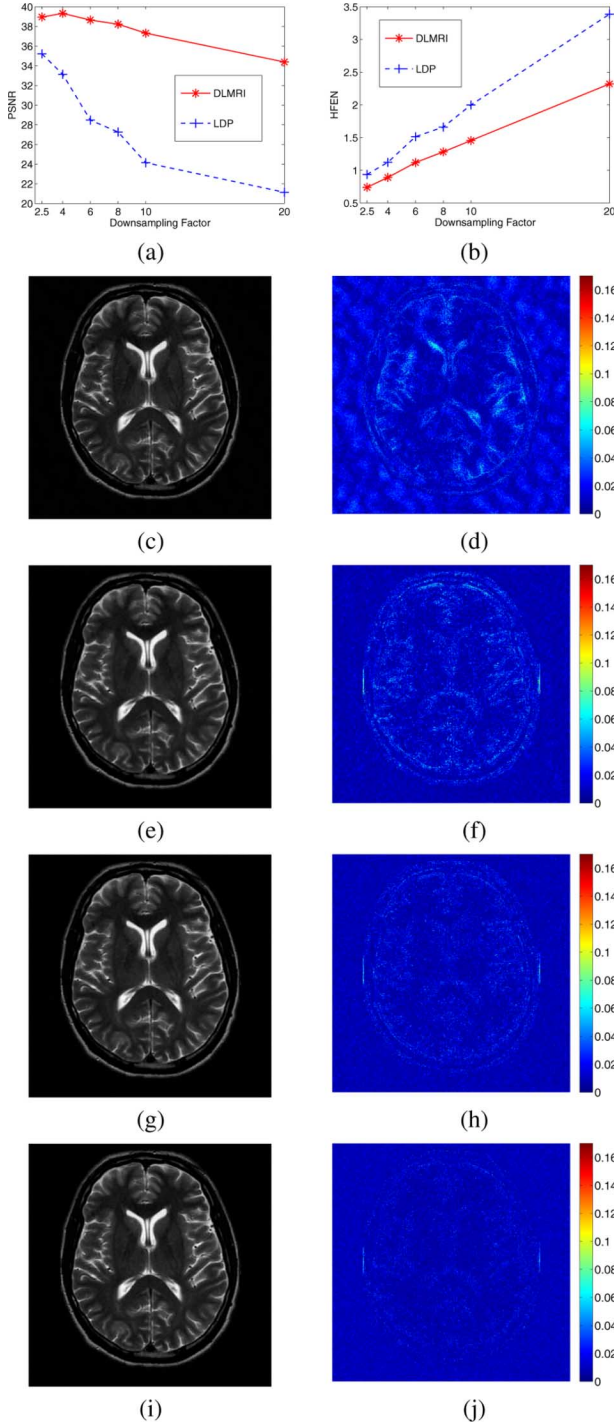


Fig. 12. Undersampling limit. (a) PSNR versus undersampling factor for DLMRI and LDP [16], [61]. (b) HFEN versus undersampling factor for DLMRI and LDP [16], [61]. (c) Reconstruction using LDP [16], [61] with Wavelets and TV at 2.5 fold undersampling. (d) Magnitude of reconstruction error for (c). (e) Reconstruction using DLMRI at 10 fold undersampling. (f) Magnitude of reconstruction error for (e). (g) Reconstruction using DLMRI at 6-fold undersampling. (h) Magnitude of reconstruction error for (g). (i) Reconstruction using DLMRI at 4 fold undersampling. (j) Magnitude of reconstruction error for (i).

The PSNR of DLMRI is high even at very high undersampling factors such as 20, indicating good removal of aliasing and noise. On the other hand, the PSNR of the LDP [16], [61]

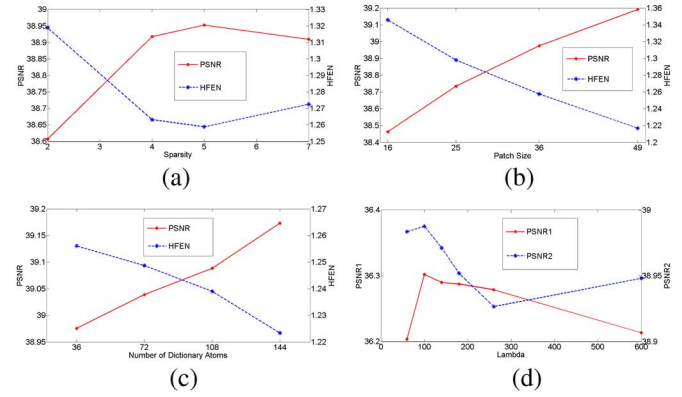


Fig. 13. Parameter evaluation. (a) PSNR and HFEN versus sparsity. (b) PSNR and HFEN versus patch size. (c) PSNR and HFEN versus overcompleteness of dictionary. (d) PSNR versus λ at $\sigma = 18.8$ (PSNR1), and $\sigma = 0.01$ (PSNR2).

method is comparable to those of DLMRI only at a low undersampling factor of 2.5. This indicates that the LDP [16], [61] method is unable to remove aliasing and noise sufficiently well at higher undersampling factors. The HFEN values for the LDP [16], [61] method are also higher than the corresponding values for DLMRI at all undersampling factors. HFEN for the LDP [16], [61] method at 2.5 fold undersampling is comparable to that of DLMRI at 4 or 6 fold undersampling.

The reconstruction for the LDP [16], [61] method at 2.5 fold undersampling is shown along with the magnitude of the reconstruction error. Some structure is seen in the error indicating loss of features. The reconstruction for DLMRI is observed to be free of aliasing and noise even at 10 fold undersampling. However, there is some error observed at the edges which can be inferred from the higher value of HFEN at this factor. The reconstructions with DLMRI at 4 or 6 fold undersampling can be seen to be almost error-free. The results indicate that DLMRI can achieve almost 2.5–4 times higher undersampling factors than existing CSMRI methods at comparable reconstruction errors.

E. Parameter Evaluation

In this experiment, the sensitivity of the algorithm to parameter settings was evaluated by varying one parameter at a time while keeping the rest fixed at their nominal values. The reference image in Fig. 6 was used for the evaluation with 2D random sampling and 10 fold undersampling. The parameters evaluated were the patch size (n), sparsity threshold (T_0), weight (λ), and the overcompleteness of the dictionary (K). PSNR and HFEN are plotted in Fig. 13 over these parameters. The overlap stride (r), and training fraction (δ) were observed to work well at their nominal values, and are not studied separately.

In Fig. 13, when the sparsity threshold is increased from 2 to 5, both PSNR and HFEN improve. However, at higher sparsity levels such as 7, the performance degrades. The poorer performance at the low sparsity level of 2 is due to the loss of resolution and higher sparse coding residuals encountered at low sparsity. At high sparsity levels such as 7, the algorithm begins to allow aliasing artifacts in the reconstruction thereby degrading performance. The performance with respect to patch size conforms to expectations. As the patch size is increased from 4×4 to 7×7 , both PSNR and HFEN improve. However, the amount

of improvement from patch size of 6×6 to 7×7 or higher is small as compared to going from 4×4 to 6×6 . The increase in patch size also increases computation thereby preventing us from working at patch sizes that are too high. It is to be noted that the nominal values for T_0 and K depend on n and hence, the actual numerical values change with n . The change in PSNR and HFEN with increase in overcompleteness is rather small indicating that square dictionaries can suffice in practise. The K-SVD learning scheme for the overcomplete cases was initialized using a combination of left singular vectors of the training patches and some training patches.

We evaluated λ with complex white Gaussian noise at two different levels: $\sigma 18.8$, and $\sigma 0.01$. At each of these noise levels, the variation of PSNR is plotted versus $\lambda \in [60 \ 600]$. The changes in PSNR are seen to be small in that range and the values are quite good around $\lambda = 140$ used by us. The same value of $\lambda = 140$ works well at the two very different noise levels spanning a range of 65 dB. This is due to the noise-adapted weighting that we use (λ/σ). The slow variation in PSNR with λ also indicates that a rough estimate for the noise level σ would work when the actual value is unknown. The drop in reconstruction PSNR when σ is increased from 0.01 to 18.8 is only about 2.7 dB which demonstrates that DLMRI is reasonably robust to noise.

The plots of Fig. 13 indicate that the “nominal” parameter values work reasonably well. They also show that the algorithm is not overtly sensitive to the parameters and can be used with little or no tuning. The various experimental results demonstrated using different sampling schemes, noise levels, undersampling factors, and images also indicate the good performance of the set parameters.

VI. CONCLUSION AND FUTURE WORK

In this work, a novel adaptive reconstruction framework exploiting image patch-based sparsity has been presented. The patch-based dictionary is obtained directly using the sampled k-space data and is thus adapted to the specific image instance. The alternating algorithm presented here learns the dictionary and removes aliasing and noise in one step, and enforces data fidelity in the next step. Various experimental results demonstrate the superior performance of the algorithm in both noiseless and noisy scenarios. The performance is demonstrated using a variety of sampling trajectories and k-space undersampling factors. The algorithm usually converges in a small number of iterations and provides highly accurate reconstructions at high undersampling factors. It is also robust to parameter selection. The dictionary learning step of the algorithm can also be additionally initialized with a dictionary learnt from reference image(s), in order to reduce the number of iterations required for convergence, and thus accelerating the algorithm further. The design of optimal sampling schemes for DLMRI is a subject for future study. The proposed framework can also be extended to other imaging applications. Work in this direction is ongoing and will be presented in the near future.

REFERENCES

- [1] K. P. Pruessmann, “Encoding and reconstruction in parallel MRI,” *NMR Biomed.*, vol. 19, no. 3, pp. 288–299, 2006.
- [2] Z. Liang and P. Lauterbur, *Principles of Magnetic Resonance Imaging: A Signal Processing Perspective*. New York: Wiley-IEEE, 1999.
- [3] N. Aggarwal and Y. Bresler, “Patient-adapted reconstruction and acquisition dynamic imaging method (PARADIGM) for MRI,” *Inverse Problems*, vol. 24, no. 4, pp. 045015–1–045015–29, 2008.
- [4] B. Sharif, J. A. Derbyshire, A. Z. Faranesh, and Y. Bresler, “Patient-adaptive reconstruction and acquisition in dynamic imaging with sensitivity encoding (PARADISE),” *Magn. Reson. Med.*, vol. 64, no. 2, pp. 501–513, 2010.
- [5] E. Candès, J. Romberg, and T. Tao, “Robust uncertainty principles: Exact signal reconstruction from highly incomplete frequency information,” *IEEE Trans. Inf. Theory*, vol. 52, no. 2, pp. 489–509, Feb. 2006.
- [6] D. Donoho, “Compressed sensing,” *IEEE Trans. Inf. Theory*, vol. 52, no. 4, pp. 1289–1306, Apr. 2006.
- [7] E. Candès and T. Tao, “Decoding by linear programming,” *IEEE Trans. Inf. Theory*, vol. 51, no. 12, pp. 4203–4215, Dec. 2005.
- [8] P. Feng and Y. Bresler, “Spectrum-blind minimum-rate sampling and reconstruction of multiband signals,” in *ICASSP*, May 1996, vol. 3, pp. 1689–1692.
- [9] Y. Bresler and P. Feng, “Spectrum-blind minimum-rate sampling and reconstruction of 2-D multiband signals,” in *Proc. 3rd IEEE Int. Conf. Image Process. (ICIP’96)*, Sep. 1996, pp. 701–704.
- [10] P. Feng, “Universal spectrum blind minimum rate sampling and reconstruction of multiband signals,” Ph.D. dissertation, Univ. Illinois, Urbana-Champaign, Mar. 1997.
- [11] R. Venkataramani and Y. Bresler, “Further results on spectrum blind sampling of 2D signals,” in *Proc. IEEE Int. Conf. Image Proc. (ICIP)*, Oct. 1998, vol. 2, pp. 752–756.
- [12] Y. Bresler, M. Gastpar, and R. Venkataramani, “Image compression on-the-fly by universal sampling in Fourier imaging systems,” in *Proc. 1999 IEEE Inf. Theory Workshop Detection, Estimation, Classification, Imag.*, Feb. 1999, p. 48.
- [13] M. Gastpar and Y. Bresler, “On the necessary density for spectrum-blind nonuniform sampling subject to quantization,” in *ICASSP*, Jun. 2000, vol. 1, pp. 348–351.
- [14] J. C. Ye, Y. Bresler, and P. Moulin, “A self-referencing level-set method for image reconstruction from sparse Fourier samples,” *Int. J. Comput. Vis.*, vol. 50, no. 3, pp. 253–270, Dec. 2002.
- [15] Y. Bresler, “Spectrum-blind sampling and compressive sensing for continuous-index signals,” in *Proc. 2008 Inf. Theory Appl. Workshop Conf.*, 2008, pp. 547–554.
- [16] M. Lustig, D. Donoho, and J. Pauly, “Sparse MRI: The application of compressed sensing for rapid MR imaging,” *Magn. Reson. Med.*, vol. 58, no. 6, pp. 1182–1195, 2007.
- [17] M. Lustig, J. M. Santos, D. L. Donoho, and J. M. Pauly, “k-t SPARSE: High frame rate dynamic MRI exploiting spatio-temporal sparsity,” in *Proc. ISMRM*, 2006, p. 2420.
- [18] R. Chartrand, “Fast algorithms for nonconvex compressive sensing: MRI reconstruction from very few data,” in *Proc. IEEE Int. Symp. Biomed. Imag. (ISBI)*, 2009, pp. 262–265.
- [19] J. Trzasko and A. Manduca, “Highly undersampled magnetic resonance image reconstruction via homotopic l_0 -minimization,” *IEEE Trans. Med. Imag.*, vol. 28, no. 1, pp. 106–121, Jan. 2009.
- [20] Y. Kim, M. S. Nadar, and A. Bilgin, “Wavelet-based compressed sensing using gaussian scale mixtures,” in *Proc. ISMRM*, 2010, p. 4856.
- [21] C. Qiu, W. Lu, and N. Vaswani, “Real-time dynamic MR image reconstruction using Kalman filtered compressed sensing,” in *Proc. IEEE Int. Conf. Acoustics, Speech, Signal Process.*, 2009, pp. 393–396.
- [22] S. Ma, W. Yin, Y. Zhang, and A. Chakraborty, “An efficient algorithm for compressed MR imaging using total variation and wavelets,” in *Proc. IEEE Int. Conf. Comput. Vis. Pattern Recognit. (CVPR)*, 2008, pp. 1–8.
- [23] 2009, American Radiology Services [Online]. Available: <http://www3.americanradiology.com/pls/web1/wwwimgal.vmg/>
- [24] M. Aharon, M. Elad, and A. Bruckstein, “K-SVD: An algorithm for designing overcomplete dictionaries for sparse representation,” *IEEE Trans. Signal Process.*, vol. 54, no. 11, pp. 4311–4322, Nov. 2006.
- [25] K. Engan, S. Aase, and J. Hakon-Husoy, “Method of optimal directions for frame design,” in *Proc. IEEE Int. Conf. Acoustics, Speech, Signal Process.*, 1999, pp. 2443–2446.
- [26] M. Elad and M. Aharon, “Image denoising via sparse and redundant representations over learned dictionaries,” *IEEE Trans. Image Process.*, vol. 15, no. 12, pp. 3736–3745, Dec. 2006.
- [27] J. Mairal, M. Elad, and G. Sapiro, “Sparse representation for color image restoration,” *IEEE Trans. Image Process.*, vol. 17, no. 1, pp. 53–69, Jan. 2008.

- [28] M. Protter and M. Elad, "Image sequence denoising via sparse and redundant representations," *IEEE Trans. Image Process.*, vol. 18, no. 1, pp. 27–36, Jan. 2009.
- [29] M. Aharon and M. Elad, "Sparse and redundant modeling of image content using an image-signature-dictionary," *SIAM J. Imag. Sci.*, vol. 1, no. 3, pp. 228–247, 2008.
- [30] J. Mairal, G. Sapiro, and M. Elad, "Learning multiscale sparse representations for image and video restoration," *SIAM Multiscale Model. Simulat.*, vol. 7, no. 1, pp. 214–241, 2008.
- [31] G. Yu, G. Sapiro, and S. Mallat, "Image modeling and enhancement via structured sparse model selection," in *Proc. IEEE Int. Conf. Image Process. (ICIP)*, Sep., 2010, pp. 1641–1644.
- [32] C. Kervrann and J. Boulanger, "Local adaptivity to variable smoothness for exemplar-based image regularization and representation," *Int. J. Comput. Vis.*, vol. 79, no. 1, pp. 45–69, 2008.
- [33] J. A. Tropp, "Greed is good: Algorithmic results for sparse approximation," *IEEE Trans. Inf. Theory*, vol. 50, no. 10, pp. 2231–2242, Oct. 2004.
- [34] D. L. Donoho, "For most large underdetermined systems of linear equations the minimal l_1 -norm solution is also the sparsest solution," *Comm. Pure Appl. Math.*, vol. 59, pp. 797–829, 2004.
- [35] D. L. Donoho, M. Elad, and V. N. Temlyakov, "Stable recovery of sparse overcomplete representations in the presence of noise," *IEEE Trans. Inf. Theory*, vol. 52, no. 1, pp. 6–18, Jan. 2006.
- [36] I. F. Gorodnitsky, J. George, and B. D. Rao, "Neuromagnetic source imaging with FOCUSS: A recursive weighted minimum norm algorithm," *Electroencephalogr. Clin. Neurophysiol.*, vol. 95, pp. 231–251, 1995.
- [37] G. Harikumar and Y. Bresler, "A new algorithm for computing sparse solutions to linear inverse problems," in *Proc. IEEE Int. Conf. Acoustics, Speech, Signal Process.*, May 1996, pp. 1331–1334.
- [38] Y. Bresler, C. Couvreur, and G. Harikumar, "Fast optimal and sub-optimal algorithms for sparse solutions to linear inverse problems," in *Proc. IEEE Int. Conf. Acoust. Speech, Sig. Proc.*, Apr. 1998, vol. 3, pp. 1877–1880.
- [39] G. Harikumar, "Blind image deconvolution from multiple blurs, and sparse approximation," Ph.D. dissertation, Univ. Illinois, Urbana-Champaign, Mar. 1997.
- [40] R. Chartrand, "Exact reconstruction of sparse signals via nonconvex minimization," *IEEE Signal Process. Lett.*, vol. 14, no. 10, pp. 707–710, Oct. 2007.
- [41] U. Gamper, P. Boesiger, and S. Kozerke, "Compressed sensing in dynamic MRI," *Magn. Reson. Med.*, vol. 59, no. 2, pp. 365–373, 2008.
- [42] H. Jung, K. Sung, K. S. Nayak, E. Y. Kim, and J. C. Ye, "k-t FOCUSS: A general compressed sensing framework for high resolution dynamic MRI," *Magn. Reson. Med.*, vol. 61, no. 1, pp. 103–116, 2009.
- [43] B. Wu, R. Watts, R. Millane, and P. Bones, "An improved approach in applying compressed sensing in parallel MR imaging," in *Proc. ISMRM*, 2009, p. 4595.
- [44] B. Liu, F. M. Seibert, Y. Zou, and L. Ying, "SparseSENSE: Randomly-sampled parallel imaging using compressed sensing," in *Proc. ISMRM*, 2008, p. 3154.
- [45] G. Adluru and E. V. R. DiBella, "Reordering for improved constrained reconstruction from undersampled k-space data," *J. Biomed. Imag.*, vol. 2008, pp. 1–12, 2008.
- [46] Y. Kim, M. I. Altbach, T. P. Trouard, and A. Bilgin, "Compressed sensing using dual-tree complex wavelet transform," in *Proc. ISMRM*, 2009, p. 2814.
- [47] X. Qu, D. Guo, Z. Chen, and C. Cai, "Compressed sensing MRI based on nonsubsampling contourlet transform," in *Proc. IEEE Int. Symp. IT Med. Edu.*, 2008, pp. 693–696.
- [48] X. Qu, X. Cao, D. Guo, C. Hu, and Z. Chen, "Combined sparsifying transforms for compressed sensing MRI," *Electron. Lett.*, vol. 46, no. 2, pp. 121–123, 2010.
- [49] X. Qu, W. Zhang, D. Guo, C. Cai, S. Cai, and Z. Chen, "Iterative thresholding compressed sensing MRI based on contourlet transform," *Inverse Problems Sci. Eng.*, Jun. 2010.
- [50] J. Trzasko, A. Manduca, and E. Borisch, "Robust kernel methods for sparse MR image reconstruction," in *Proc. Med. Image Comput. Computer-Assist. Intervent. (MICCAI 2007)*, 2007, pp. 809–816.
- [51] J. Trzasko, A. Manduca, and E. Borisch, "Sparse MRI reconstruction via multiscale l_0 -continuation," in *Proc. IEEE/SP 14th Workshop Stat. Signal Process.*, 2007, pp. 176–180.
- [52] M. Yaghoobi, T. Blumensath, and M. Davies, "Dictionary learning for sparse approximations with the majorization method," *IEEE Trans. Signal Process.*, vol. 57, no. 6, pp. 2178–2191, Jun. 2009.
- [53] B. A. Olshausen and D. J. Field, "Emergence of simple-cell receptive field properties by learning a sparse code for natural images," *Nature*, vol. 381, no. 6583, pp. 607–609, 1996.
- [54] R. Rubinstein, A. M. Bruckstein, and M. Elad, "Dictionaries for sparse representation modeling," *Proc. IEEE*, vol. 98, no. 6, pp. 1045–1057, 2010.
- [55] I. Tosic, I. Jovanovic, P. Frossard, M. Vetterli, and N. Duric, "Ultrasound tomography with learned dictionaries," in *Proc. IEEE Int. Conf. Acoust., Speech Signal Process.*, 2010, pp. 5502–5505.
- [56] A. Bilgin, Y. Kim, F. Liu, and M. S. Nadar, "Dictionary design for compressed sensing MRI," in *Proc. ISMRM*, 2010, p. 4887.
- [57] Y. Chen, X. Ye, and F. Huang, "A novel method and fast algorithm for MR image reconstruction with significantly under-sampled data," *Inverse Problems Imag.*, vol. 4, no. 2, pp. 223–240, 2010.
- [58] R. Otazo and D. K. Sodickson, "Adaptive compressed sensing MRI," in *Proc. ISMRM*, 2010, p. 4867.
- [59] R. Gribonval and K. Schnass, "Dictionary identification—Sparse matrix-factorisation via l_1 -minimisation," *IEEE Trans. Inf. Theory* vol. 56, no. 7, pp. 3523–3539, Jul. 2010.
- [60] J. I. Jackson, C. H. Meyer, D. G. Nishimura, and A. Macovski, "Selection of a convolution function for Fourier inversion using gridding," *IEEE Trans. Med. Imag.*, vol. 10, no. 3, pp. 473–478, Sep. 1991.
- [61] M. Lustig, 2006 [Online]. Available: <http://www.stanford.edu/~mlustig/>